

Cite this: *J. Mater. Chem. A*, 2020, 8, 55Received 12th September 2019
Accepted 12th November 2019

DOI: 10.1039/c9ta10071g

rsc.li/materials-a

Electrocatalytic reduction of N₂ and nitrogen-incorporation process on dopant-free defect graphene†

Yanqiu Du,^a Cheng Jiang,^a Wei Xia,^a Li Song,^a Peng Li,^a Bin Gao,^a Chao Wu,^a Lei Sheng,^a Jinhua Ye,^b Tao Wang^{b*} and Jianping He^{b*}

The electrochemical reduction of N₂ to NH₃ under ambient conditions is a promising N₂ fixation method, which provides a new technical solution to remedy the limitations of the Haber–Bosch process. Defect engineering is considered an inspiring strategy for strong N₂ activation. Herein, we demonstrate the reduction of N₂ on dopant-free defect graphene, which was prepared *via* the molten salt method. Systematic experiments and density functional theory calculation revealed that the defect sites are the unique active sites for nitrogen adsorption and activation. The phenomenon of N incorporation into graphene using the product NH₃ from the NRR as the N source has never been reported before. This was thoroughly studied in this study, and thus serves as a unique perspective to illustrate the significance of defect sites in activating N₂.

The process of converting free nitrogen into nitrogenous compounds is known as N₂ fixation, which provides a crucial element for the survival of living organisms. As the most widely used process for N₂ fixation, the Haber–Bosch method can be performed only under high temperature and high pressure,¹ which is extremely energy-dependent and responsible for massive CO₂ emissions. Considering the urgent demand for more sustainable alternatives, many efforts have been devoted to finding cleaner ways to remedy the defects of traditional processes. The N₂ reduction reaction (NRR) is the most promising candidate, during which N₂ fixation is driven by renewable electricity.² Unfortunately, the low efficiency of the NRR is still far from satisfactory for its widespread use because it is limited by the ultrahigh stability of the N≡N bond and the competitive

hydrogen evolution reaction.³ Consequently, the development of high-performance electrocatalysts with the ability to significantly reduce the N₂ activation energy is essential for the NRR.

Recently, numerous electrocatalysts based on noble metals and transition metals showed high activity, such as Ru⁴ and MoS₂.⁵ The unsaturated d orbitals, which synergistically accept electron density from and back donate to N₂,⁶ endow transition metal catalysts with prominent performances. Notably, many transition metal catalysts are anchored on carbon nanomaterials, such as porous carbon⁷ and CNT.⁸ However, the significant contribution of dopant-free carbon substrates for the NRR has rarely been investigated.

Graphene, as an ideal platform to load electrocatalysts,⁹ is always modified *via* the introduction of heteroatoms such as nitrogen and boron to improve its application. It has been long accepted that graphene can be activated by lone-pair electrons from electron-rich dopants or vacant orbitals from electron-deficient dopants by breaking the integrity of π conjugation.^{10,11} This activation process is usually advantageous for improving catalytic activity. However, intrinsic carbon defects can produce the same effects, breaking the original electron arrangement and improving the electron transfer from the electrocatalyst to chemisorbed molecules.¹² Fortunately, a previous study proved that the edge-rich graphene is more active than the basal plane in the oxygen reduction reaction.¹³ Besides, theoretical calculations and experimental works confirmed that defective graphene is also effective for other catalytic reactions such as the OER and HER.¹⁴ This inspired us to consider whether the defects in graphene are functional for the N₂ reduction reaction.

Herein, we designed dopant-free few-layer graphene with rich defects, which was obtained by controlling the synthetic conditions, and investigated its NRR activity. The synthesized ultrathin porous graphene achieved a faradaic efficiency (FE) of 8.51% at -0.4 V *vs.* RHE for NH₃ electrosynthesis. This remarkable performance was enabled by the enhancement in defect density, higher surface area and larger pore volume. This study not only shows the feasibility of pure carbon

^aCollege of Materials Science and Technology, Jiangsu Key Laboratory of Electrochemical Energy Storage Technologies, Nanjing University of Aeronautics and Astronautics, 29 Yudao Street, Nanjing, 210016, P. R. China. E-mail: wangtao0729@nuaa.edu.cn; jianph@nuaa.edu.cn; Fax: +86 25 52112626; Tel: +86 25 52112900

^bInternational Center for Materials Nanoarchitectonics (WPI-MANA), National Institute for Materials Science (NIMS), 1-1 Namiki, Tsukuba, Ibaraki 305-0044, Japan
† Electronic supplementary information (ESI) available. See DOI: 10.1039/c9ta10071g

nanomaterials as highly efficient NRR catalysts, but also serves as a model system to investigate the origin of NRR activity in carbon-based electrocatalysts.

The process to create defects is illustrated in Fig. 1a, where freeze-dried oxidized graphite was annealed in molten salts. Molten salt-based exfoliation has been successfully applied to synthesize thin BN nanosheets from bulk materials.^{15,16} Inspired by this, we adopted this method to synthesize few-layer graphene from bulk oxidized graphite (Fig. S1†). The scanning electron microscopy (SEM) images reveal that the morphology of graphene after annealing at 800 °C, labelled as DG-800, is wrinkled and crimped (Fig. 1b and S2†), suggesting that the exfoliation process is based on its attachment to salts and subsequent peeling off (Fig. S3†).¹⁷ The morphology of graphene is sensitively dependent on the annealing temperature. When the temperature was up to 900 °C, the product DG-900 with distinct stacking was not favorable for effective utilization of its active area (Fig. S2e†). The graphene sheet was investigated by atomic force microscopy (AFM), showing

a thickness of 3 nm (Fig. 1c). Furthermore, numerous nanopores with a size in the range of 1–5 nm were observed on the surface of DG-800 in the TEM images (Fig. 1d and e) and aberration-corrected HAADF-STEM image (Fig. S4†).¹⁸ Concomitant with numerous nanopores, a higher edge exposure will offer more active sites for N₂ adsorption and activation. Contrary to that treated with molten salt, obvious defects were not found in the pristine graphene (denoted as PG), and its graphene sheet was multi-layer (Fig. S5†) and unbroken (Fig. 1f and g). According to the N₂-physisorption measurements, the Brunauer–Emmett–Teller (BET) specific surface area of DG-800 is 420.20 m² g⁻¹, which is much higher than that of PG (78.33 m² g⁻¹). The inset pore size distribution curves indicate that the size of the mesopores is centered at 3.4 nm and the mesopore volume was significantly boosted, which is mainly attributed to the etching effect of the molten salt (Fig. 2a and Table S1†). With the aid of the molten salt, the multi-layer bulk graphene was exfoliated into few-layer ultrathin porous nanosheets with abundant mesopores and exposed edges. These features

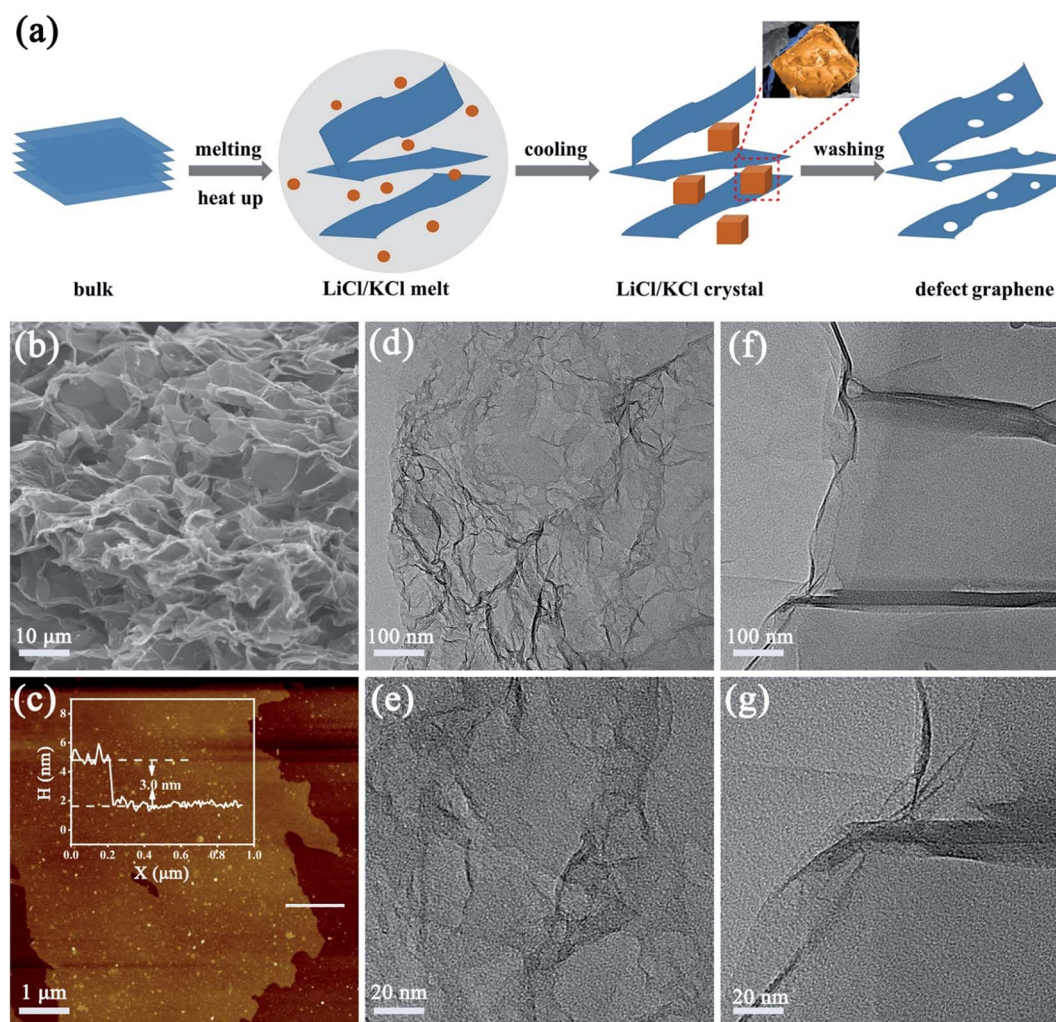


Fig. 1 (a) Schematic illustration of the synthesis of defect graphene. (b) SEM image of defect graphene DG-800, where DG-800 is the sample treated with molten salt at 800 °C. (c) AFM image of DG-800. (d and e) TEM images of DG-800 at different magnifications. (f and g) TEM images of PG at different magnifications, where PG is the sample treated without molten salt.

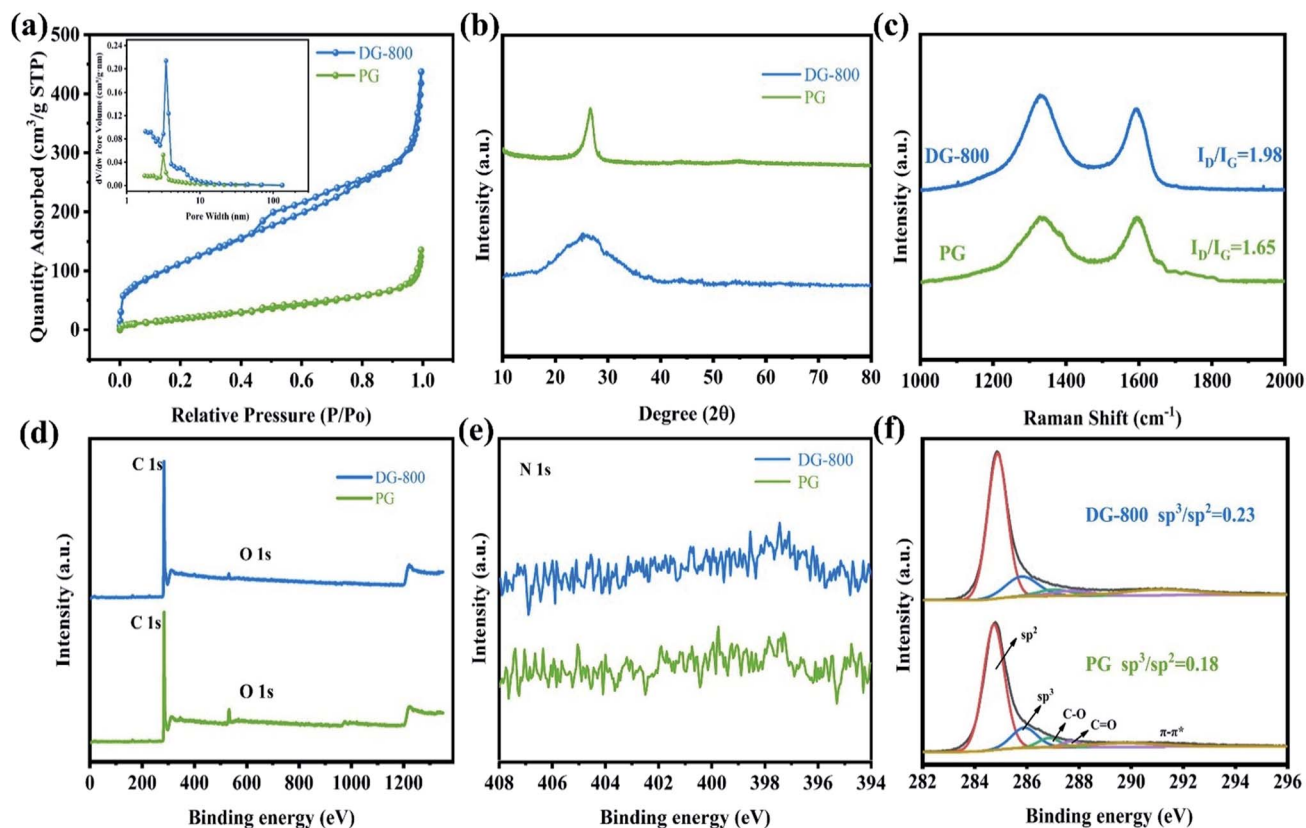


Fig. 2 (a) Nitrogen adsorption–desorption isotherms and the inset corresponding pore size distribution of the catalyst DG-800 and PG. (b) XRD spectra of DG-800 and PG. (c) Raman spectra of PG and DG-800. (d) Full XPS spectra of DG-800 and PG. (e) N 1s XPS spectrum of DG-800. (f) C 1s XPS spectra of DG-800 and PG.

revealed by microscopy are beneficial for the maximum inherent activity.

The defect-induced alteration in local structure was further characterized. Primarily, the X-ray diffraction (XRD) characterization of PG and representative defect graphene is presented in Fig. 2b. The diffraction peak at 26.6° changes from a sharp peak to a broader peak due to the destruction of the long-range order in the atomic arrangements after annealing.¹⁹ The I_D/I_G ratio of PG and DG-800 in the Raman spectra, which is a powerful tool to quantify disorder, increased from 1.65 to 1.98, implying a higher defect concentration and coinciding well with the XRD measurements and TEM images (Fig. 2c).²⁰ X-ray photoelectron spectroscopy (XPS) (Fig. 2d) indicated that only carbon and oxygen were present in the sample. Since no peaks for K^+ and Li^+ were initially detected by XPS (as shown in Fig. 2d), we then proceeded to use ICP, a sensitive technique suitable for trace elements, to detect the metallic impurities of K^+ and Li^+ . In DG-800, the amount of K and Li was found to be 0.048 wt% and 0.0086 wt%, respectively, which are too low to be electroactive. Considering permanganates are used in the Hummers' method, the analysis of residual Mn was also conducted, which was determined to be only 0.043 wt%. More specifically, no obvious peak can be detected on the N 1s XPS spectra (Fig. 2e). Thus, the problem of nitrogen species causing false positive results can be avoided.²¹ The asymmetric high-resolution C 1s spectra were

deconvoluted into five peaks, where the peaks at 284.75 and 285.9 eV correspond to sp^2 and sp^3 carbon,^{22,23} respectively (Fig. 2f). The ratio of sp^3 to sp^2 carbons in DG-800 was determined to be approximately 0.23, which is higher than that in PG and another quantitative description of more defects in DG-800.¹³ Thus, the above spectroscopic characterization fully confirms the successful preparation of defect graphene.

The NRR activity of defect graphene was preliminarily probed *via* the noticeable difference between Ar- and N_2 -saturated electrolytes in LSV tests (Fig. 3a). Considering the increase in current density and the existence of N_2 , the N_2 reduction reaction is the most convincing reason for the above difference. Inspired by this, further NRR tests were performed to confirm the electrocatalytic activity of the defect graphene. All the NRR electrochemical tests were performed in an H-type cell with a continuous N_2 flow, which was separated by a Nafion membrane. To clean ammonia from the membrane in between tests, the Nafion membrane was retreated in 3% H_2O_2 and 0.5 M H_2SO_4 for 1 h at $80^\circ C$ after the test. The NH_3 produced in the chronoamperometry tests were analyzed by Nessler's reagent and indophenol blue together, thus ensuring the accuracy of the results (the calibration curves are shown in Fig. S6 and S7†). Furthermore, carefully controlling the conditions ensured that the calculated NH_4^+ had an acceptable error, with a standard deviation of <2% (Table S2†). The absorbance of the electrolyte

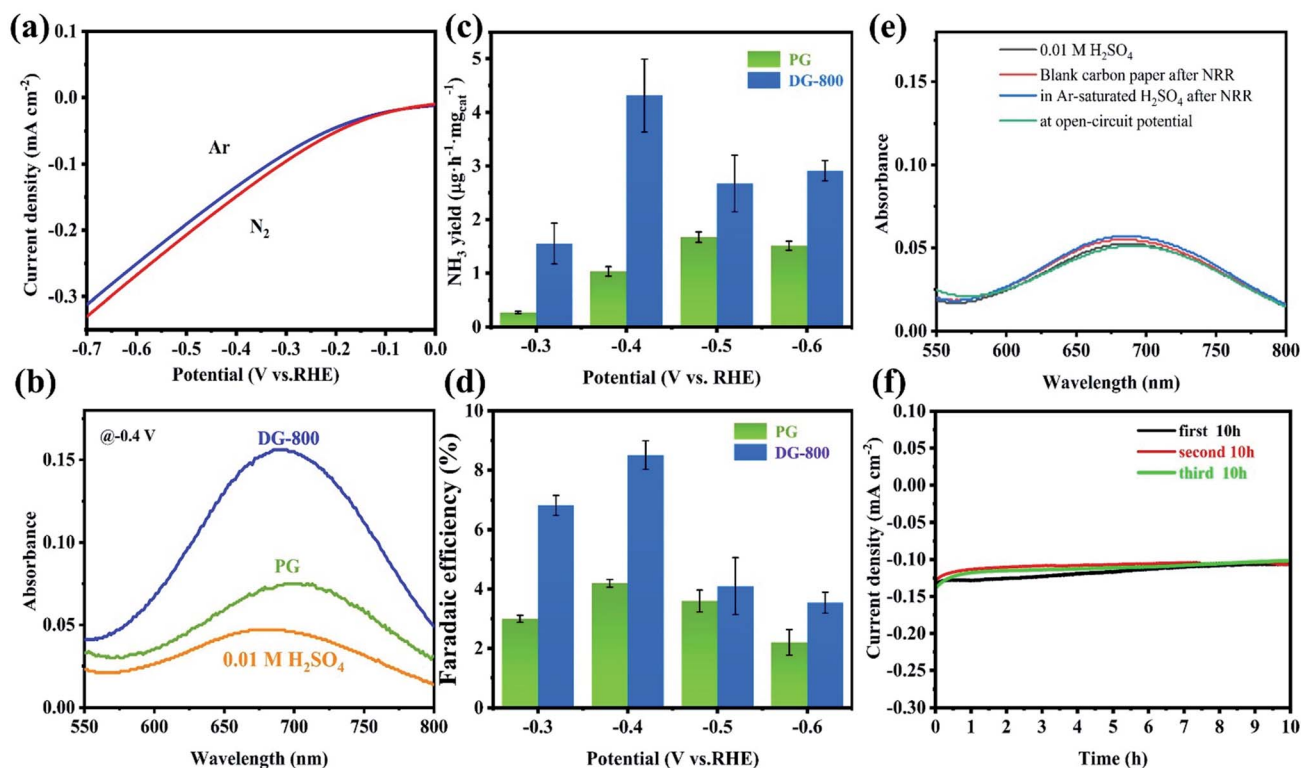


Fig. 3 (a) Linear sweep voltammetry curves of DG-800 in Ar- and N₂-saturated electrolyte. (b) UV-vis spectra of the electrolytes after NRR at -0.4 V vs. RHE for 2 h, where pristine electrolyte with indophenol indicator was used as a reference (yellow line). (c) NH₃ yield rate at various potentials. (d) Faradaic efficiency at various potentials. (e) UV-vis absorption spectra of the electrolytes in the control experiment stained with indophenol indicator after 2 h electrolysis. (f) Stability test of the DG-800 catalyst in N₂-saturated 0.01 M H₂SO₄ at -0.4 V vs. RHE under long-time electrolysis.

catalyzed by DG-800 was overwhelmingly enhanced compared with that of PG, indicating the better performance of DG-800 toward NH₃ synthesis (Fig. 3b and S8†). The introduction of mesoporosity and accessible defect sites in DG-800, acting as channels for the reaction medium,²⁴ greatly favored the electrocatalytic activity. By contrast, PG was a poor catalyst towards the NRR. More specific performances are presented in Fig. 3c and d, where it can be seen that the faradaic efficiency (FE) and NH₃ yield both increased with an increase in potential up to -0.4 V vs. RHE and both have peak values, and then decreased for potentials < -0.4 V vs. RHE. The degradation of the performances at a more negative potential can be explained by the competing hydrogen evolution reaction (HER), in which more protons occupy the active sites.²⁵ Subsequently, we studied the effect of the defect density on NRR activity by comparing the properties of the graphene synthesized at different temperatures (Fig. S9†). DG-800 achieved the best performance, NH₃ yield rate (4.31 μg h⁻¹ mg_{cat}⁻¹) and FE (8.51%). Consistent with Fig. S10,† we found that the defect density positively affected the NRR process. Besides, we further performed the method reported by Watt and Chrisp to detect the side product of N₂H₄ (the calibration curve is shown in Fig. S11†). As illustrated in Fig. S12,† even a negligible gap between the pristine electrolyte and electrolytes after NRR could not be detected. Therefore, it is reasonable to conclude that no N₂H₄ was produced, indicating

the high selectivity of the electrocatalyst. Considering the possible existence of NO_x residue such as NO₃⁻ in the electrolyte after the chronoamperometry tests at -0.4 V for 2 h, DG-800 as the catalyst was analyzed using an ion chromatography (IC) to verify the presence of nitrate. The IC spectra of the electrolyte after being tested and NO₃⁻ at different concentrations are provided in Fig. S13.† The peak area of the electrolyte was barely visibly, indicating negligible NO₃⁻ was present, thus excluding NH₃ oxidation and the influence of NO₃⁻ on the ammonia yield. To unambiguously confirm the source of ammonia, a series of control experiments were implemented. Blank carbon paper was used as the electrode and the N₂ flow was replaced by an Ar flow, and the absorption spectra showed no obvious difference with the pristine electrolyte (Fig. 3e), that is, no NH₄⁺ was generated. The former experiment made it clear that the synthesized graphene, rather than carbon paper, was the catalyst for the NRR. In the latter case, we did not detect NH₄⁺ in the Ar-saturated electrolyte, which lacked a nitrogen source for synthesizing ammonia since the electrocatalyst was nitrogen-free.

To evaluate the stability, a durability test consisting of three cycles of 10 h chronoamperometric tests at -0.4 V vs. RHE was conducted (Fig. 3f). The current density was well maintained at around 0.1 mA cm⁻² at the end of each cycle, showing little degradation. The key performance metrics after three cycles of

FE (7.24%) and NH_3 yield rate ($1.84 \mu\text{g h}^{-1} \text{mg}_{\text{cat}}^{-1}$) were still at a high level for a carbon-based material without any heteroatoms or transition metals. This remarkable performance clearly demonstrates the superiority of DG-800 for the NRR.

The FT-IR spectra of the catalysts after the NRR allowed us to directly trace the protonation of N_2 on the electrocatalyst surface (Fig. 4a). As reported in the literature, the two sharp peaks at 2930 cm^{-1} and 2850 cm^{-1} are attributed to the characteristic H–N–H stretching of NH_4^+ .²⁶ The intensities of these two bands increased with time, suggesting an increase in the production of NH_3 .²⁶ Contrary to the blank carbon paper, a new band at 1459 cm^{-1} was observed, which is related to the bending vibration of H–N–H in the intermediates and NH_3 species.²⁷ The appearance of H–N–H bending and stretching bands implies that proton–electron pairs transferred to the adsorbed N_2 and reaction intermediates. When PG was used as the electrocatalyst, the characteristic stretching bands of H–N–H at 2930 cm^{-1} and 2850 cm^{-1} on the electrode surface were not evident until the reaction time was 10 h (Fig. S14†). This result is due to the low NRR activity of PG.

XPS measurements, which give fresh insight into N_2 fixation, were conducted on the carbon paper with DG-800 after the NRR test, and as a control, the same film sample before the NRR test. As shown in Fig. 4b, the XPS spectra on the film sample before the test revealed C, O, F, and S signals without N, where F and S originate from the Nafion binder ($\text{C}_9\text{HF}_{17}\text{O}_5\text{S}$). Apparently, a clear N signal on the sample after the NRR test was detected, whereas there was no N signal on the control sample. The XPS data for nitrogen content (Table S3†) distinctly changed from

0 to 1.4%, providing solid spectroscopic evidence of the successful fixation of N_2 on DG-800. Further, the N 1s spectrum was deconvoluted into three peaks (Fig. 4c) corresponding to NH_4^+ (402.5 eV),^{28–30} graphitic N (401.2 eV),^{31,32} and pyrrolic N (400.1 eV).³³ Thus, the reduction of N_2 to ammonia on DG-800 was verified again by the peak at around 402.5 eV. The edges and defect sites afford C atoms that are much more chemically reactive than that in the plane of perfect graphene for the formation of nitrogen-containing groups.³⁴

To further confirm that defect sites are responsible for the enhanced performance, the XPS results for PG and DG-800 were compared. As presented in Fig. S16,† only a small amount of N was doped in PG, mostly in the form of pyrrolic N. Combined with the nearly perfect basal plane of PG, it is credible that N was predominantly incorporated into the edges of PG, an unavoidable defective domain in graphene. Considering the NRR, the basal plane was found to be inert and N_2 molecules cannot be effectively absorbed.³⁵ This comparison highlights the necessity of creating a favorable environment, such as defect sites, for molecular chemisorption. In addition, DFT calculations were employed to describe the N_2 adsorption and activation on PG and defect sites of DG, in which both side-on and end-on configurations were considered. N_2 adsorption on DG is stronger than that on PG due to the more negative energy value of DG,³⁶ which manifests that the NRR activity benefits from the defects in DG (Fig. 4d and e). The N_2 molecules on the edge of DG are the most active, where the N–N bond is elongated to 1.116 Å, resulting in more efficient charge transfer.

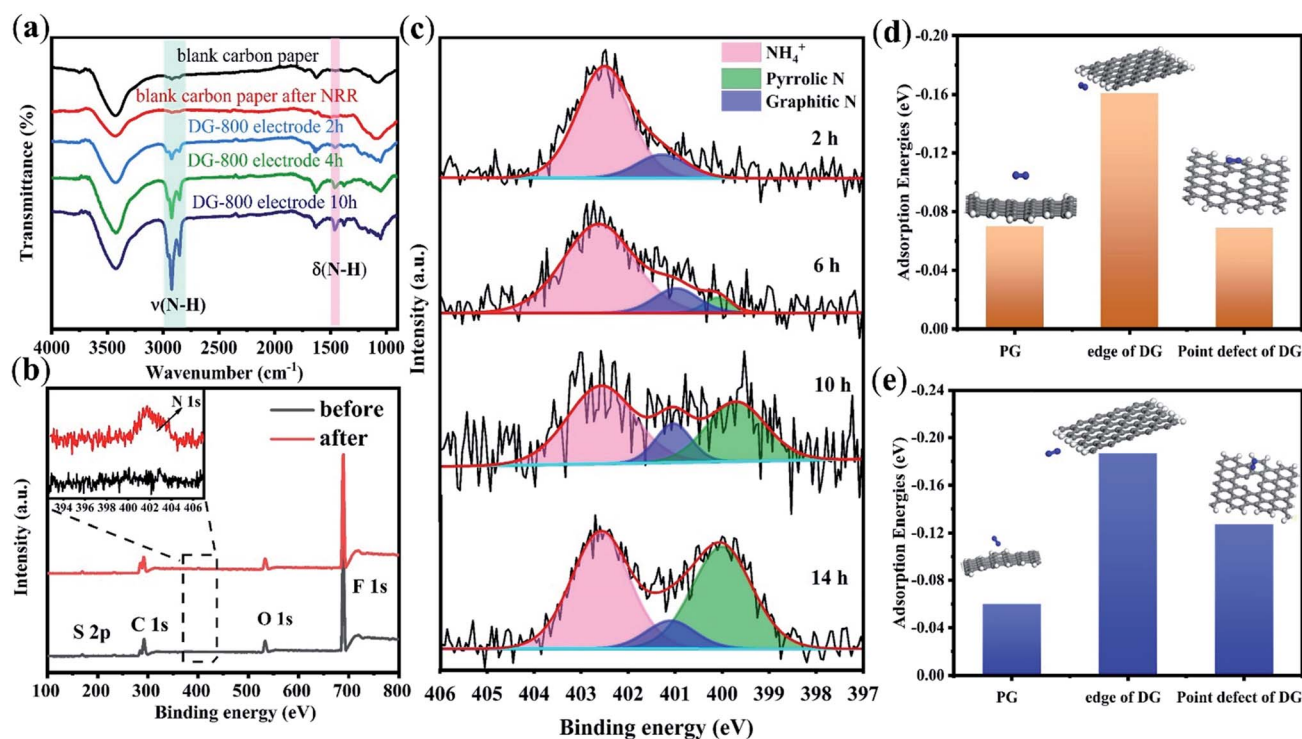


Fig. 4 (a) FT-IR spectra of blank electrode and DG-800 electrode after different reaction times. (b) Full XPS spectra and N 1s spectra (the inset) of the DG-800 electrode before and after the NRR. (c) N 1s spectra of the DG-800 electrode after different reaction times. (d) Adsorption energies (E_{ads} , eV) of N_2 molecule with the side-on configuration. (e) Adsorption energies (E_{ads} , eV) of the N_2 molecule with the end-on configuration.

Next, the evolution of nitrogen species during the reaction was monitored to study the reaction mechanism (Fig. 4c). As illustrated in Fig. S17,† we speculated that the possible configurations to form pyrrolic N and graphitic N are armchair edges and point defects, respectively. Obviously, the possible defect sites for N-dopants are much more than the two mentioned above, which are still challenging to exactly identify.³⁷ Thus, we focused on the edge sites and point defects to study the process concomitant with the NRR. On one hand, the peak of graphitic N appeared with nearly a stable area, which is associated with a decrease in the amount of point defects available for the incorporation of N atoms as the reaction proceeds (Fig. 4c). This implies that point defects are active in the primary stage. Then, once the point defects are “saturated” with N atoms, these sites are not active anymore. A previous study also reported that graphitic nitrogen is NRR-inactive since it is difficult for N₂ to adsorb on graphitic N-doped carbon.³⁸ On the other hand, pyrrolic N shows constant improvement with time (Fig. 4c and Table S4†). Mostly originating from rich edges, it can be predicted that more and more pyrrolic nitrogen will be detected as electrolysis continues.

Lastly, we supposed that the yielded NH₃, instead of N₂, serves as the nitrogen source for N doping. Then, a parallel experiment was designed to answer the above conjecture, which was carried out by replacing the N₂ flow and H₂SO₄ electrolyte with an Ar flow and (NH₄)₂SO₄ electrolyte, respectively, while keeping the reaction time (6 h) and catalyst (DG-800) constant. As expected, pyrrolic and graphitic N emerged in the parallel experiment (Fig. S18†), where NH₄⁺ was the only nitrogen source for the generation of pyrrolic and graphitic N. Thus, the formation of nitrogen-containing groups can be understood as follows, N₂ is firstly electrochemically reduced to NH₃ and then the product NH₄⁺ is incorporated into the graphene lattices in the form of pyrrolic N and graphitic N.³⁹ Specifically, the existence of pyrrolic N and graphitic N is additional proof of the N₂ reduction reaction, which represent the defect sites of graphene.

Conclusions

In summary, we demonstrated that N₂ can be efficiently reduced to NH₃ by metal-free defect graphene under ambient conditions. The defect engineering based on a salt melt endowed DG-800 with an excellent faradaic efficiency of 8.51% at -0.4 V vs. RHE for the NRR, where the well-controlled active centers of defects and edges play a crucial role. The observation of N doping in graphene after NRR provided additional proof of the successful N₂ reduction and bridges the NRR activity with the defect sites of graphene. This study highlights the significant contribution of the inherent activity of carbon in the NRR and provides different insight to understand N₂ fixation. Moving forward, precise studies such as investigation of the different roles of defect structures in NRR will be challenging but also exciting. Further, we believe that the combination of defect engineering and other promising strategies will greatly favor the development of high efficiency NRR.

Conflicts of interest

There are no conflicts to declare.

Acknowledgements

The authors express their appreciations for the financial support from the National Natural Science Foundation of China (11575084, 51602153), the Natural Science Foundation of Jiangsu Province (BK20160795), the Fundamental Research Funds for the Central Universities (No. NE2018104), and a project funded by the Priority Academic Program Development of Jiangsu Higher Education Institutions (PAPD).

Notes and references

- 1 M. Kitano, Y. Inoue, Y. Yamazaki, F. Hayashi, S. Kanbara, S. Matsuishi, T. Yokoyama, S. Kim, M. Hara and H. Hosono, *Nat. Chem.*, 2012, **4**, 934–940.
- 2 L. Li, C. Tang, B. Xia, H. Jin, Y. Zheng and S. Qiao, *ACS Catal.*, 2019, **9**, 2902–2908.
- 3 G. Chen, X. Cao, S. Wu, X. Zeng, L. Ding, M. Zhu and H. Wang, *J. Am. Chem. Soc.*, 2017, **139**, 9771–9774.
- 4 Y. Yao, H. Wang, X. Yuan, H. Li and M. Shao, *ACS Energy Lett.*, 2019, **4**, 1336–1341.
- 5 B. H. R. Surrnto, D. Wang, L. M. Azofra, M. Harb, L. Cavallo, R. Jalili, D. R. G. Mitchell, M. Chatti and D. R. MacFarlane, *ACS Energy Lett.*, 2019, **4**, 430–435.
- 6 M. Legare, G. Belanger-Chabot, R. D. Dewhurst, E. Welz, I. Krummenacher, B. Engels and H. Braunschweig, *Science*, 2018, **359**, 896–899.
- 7 W. Xia, J. Li, T. Wang, L. Song, H. Guo, H. Gong, C. Jiang, B. Gao and J. He, *Chem. Commun.*, 2018, **54**, 1623–1626.
- 8 L. Song, J. Tang, T. Wang, C. Wu, Y. Ide, J. He and Y. Yamauchi, *Chem.–Eur. J.*, 2019, **25**, 6807–6813.
- 9 H. Wang, X. Li, L. Gao, H. Wu, J. Yang, L. Cai, T. Ma, C. Tung, L. Wu and G. Yu, *Angew. Chem., Int. Ed.*, 2018, **57**, 192–197.
- 10 Y. Jiang, L. Yang, T. Sun, J. Zhao, Z. Lyu, O. Zhuo, X. Wang, Q. Wu, J. Ma and Z. Hu, *ACS Catal.*, 2015, **5**, 6707–6712.
- 11 J. Tang, J. Liu, C. Li, Y. Li, M. O. Tade, S. Dai and Y. Yamauchi, *Angew. Chem., Int. Ed.*, 2014, 588–593.
- 12 L. Tao, M. Qiao, R. Jin, Y. Li, Z. Xiao, Y. Wang, N. Zhang, C. Xie, Q. He, D. Jiang, G. Yu, Y. Li and S. Wang, *Angew. Chem., Int. Ed.*, 2019, **58**, 1019–1024.
- 13 L. Tao, Q. Wang, S. Dou, Z. Ma, J. Huo, S. Wang and L. Dai, *Chem. Commun.*, 2016, **52**, 2764–2767.
- 14 Y. Jia, L. Zhang, A. Du, G. Gao, J. Chen, X. Yan, C. L. Brown and X. Yao, *Adv. Mater.*, 2016, **28**, 9532–9538.
- 15 W. Lei, D. Portehault, R. Dimova and M. Antonietti, *J. Am. Chem. Soc.*, 2011, **133**, 7121–7127.
- 16 X. Li, X. Hao, M. Zhao, Y. Wu, J. Yang, Y. Tian and G. Qian, *Adv. Mater.*, 2013, **25**, 2200–2204.
- 17 X. Liu, N. Fechler and M. Antonietti, *Chem. Soc. Rev.*, 2013, **42**, 8237–8265.
- 18 W. Xia, J. Tang, J. Li, S. Zhang, K. C. W. Wu, J. He and Y. Yamauchi, *Angew. Chem., Int. Ed.*, 2019, **58**, 13354–13359.

- 19 C. Lv, Y. Qian, C. Yan, Y. Ding, Y. Liu, G. Chen and G. Yu, *Angew. Chem., Int. Ed.*, 2018, **57**, 10246–10250.
- 20 M. S. Dresselhaus, A. Jorio, A. G. Souza Filho and R. Saito, *Philos. Trans. R. Soc., A*, 2010, **368**, 5355–5377.
- 21 H. Jin, L. Li, X. Liu, C. Tang, W. Xu, S. Chen, L. Song, Y. Zheng and S. Z. Qiao, *Adv. Mater.*, 2019, 1902709.
- 22 Y. Wang, L. Tao, Z. Xiao, R. Chen, Z. Jiang and S. Wang, *Adv. Funct. Mater.*, 2018, **28**, 1705356.
- 23 C. Young, R. R. Salunkhe, J. Tang, C. Hu, M. Shahabuddin, E. Yanmaz, M. S. A. Hossain, J. H. Kim and Y. Yamauchi, *Phys. Chem. Chem. Phys.*, 2016, **18**, 29308–29315.
- 24 S. H. Lee, J. Kim, D. Y. Chung, J. M. Yoo, H. S. Lee, M. J. Kim, B. S. Mun, S. G. Kwon, Y. Sung and T. Hyeon, *J. Am. Chem. Soc.*, 2019, **141**, 2035–2045.
- 25 H. Cheng, L. Ding, G. Chen, L. Zhang, J. Xue and H. Wang, *Adv. Mater.*, 2018, **30**, 1803694.
- 26 J. Zheng, Y. Lyu, M. Qiao, R. Wang, Y. Zhou, H. Li, C. Chen, Y. Li, H. Zhou, S. P. Jiang and S. Wang, *Chem*, 2019, **5**, 617–633.
- 27 Y. Yao, S. Zhu, H. Wang, H. Li and M. Shao, *J. Am. Chem. Soc.*, 2018, **140**, 1496–1501.
- 28 W. Grunert, R. Feldhaus, K. Anders, E. S. Shpiro, G. V. Antoshin and K. M. Minachev, *J. Electron Spectrosc. Relat. Phenom.*, 1986, **40**, 187–192.
- 29 L. Sygellou, *Appl. Surf. Sci.*, 2019, **476**, 1079–1085.
- 30 J. L. Smith, R. G. Herman, C. R. Terenna, M. R. Galler and K. Klier, *J. Phys. Chem. A*, 2004, **108**, 39–46.
- 31 H. Tan, Y. Li, X. Jiang, J. Tang, Z. Wang, H. Qian, P. Mei, V. Malgras, Y. Bando and Y. Yamauchi, *Nano Energy*, 2017, **36**, 286–294.
- 32 J. Tang, R. R. Salunkhe, J. Liu, N. L. Torad, M. Imura, S. Furukawa and Y. Yamauchi, *J. Am. Chem. Soc.*, 2015, **137**, 1572–1580.
- 33 W. Zhang, X. Jiang, X. Wang, Y. V. Kaneti, Y. Chen, J. Liu, J. Jiang, Y. Yamauchi and M. Hu, *Angew. Chem., Int. Ed.*, 2017, **56**, 8435–8440.
- 34 X. Wang, X. Li, L. Zhang, Y. Yoon, P. K. Weber, H. Wang, J. Guo and H. Dai, *Science*, 2009, **324**, 768–771.
- 35 X. Li, T. Li, Y. Ma, Q. Wei, W. Qiu, H. Guo, X. Shi, P. Zhang, A. M. Asiri, L. Chen, B. Tang and X. Sun, *Adv. Energy Mater.*, 2018, **8**, 1801357.
- 36 X. Liu, Y. Jiao, Y. Zheng, M. Jaroniec and S. Qiao, *J. Am. Chem. Soc.*, 2019, **141**, 9664–9672.
- 37 Z. Hou, X. Wang, T. Ikeda, K. Terakura, M. Oshima, M. Kakimoto and S. Miyata, *Phys. Rev. B: Condens. Matter Mater. Phys.*, 2012, **85**, 165439.
- 38 Y. Liu, Y. Su, X. Quan, X. Fan, S. Chen, H. Yu, H. Zhao, Y. Zhang and J. Zhao, *ACS Catal.*, 2018, **8**, 1186–1191.
- 39 F. Lou, M. E. M. Buan, N. Muthuswamy, J. C. Walmsley, M. Rønning and D. Chen, *J. Mater. Chem. A*, 2016, **4**, 1233–1243.